Multiphysics Optimisation Model of an Ultra-High Temperature Storage Integrated with a Novel Solar-to-Heat-to-Power System

Alfonso Hernández[1,*], Luis Enrique Acevedo[1], Ignacio Fernández-Pacheco[1], Patricia Royo[1]

[1] *IDENER, Thermodynamics Division, Earle Ovington 8-9, Edificio Aeronautics Suppliers Village, Parque Tecnológico Aeroespacial de Andalucía, La Rinconada, Sevilla, 41300, Spain*
[*] *Corresponding author. Email: alfonso.hernandez@idener.ai*

ABSTRACT
The presented design integrates concentrated solar power (CSP) into a compact ultra-high temperature latent heat thermal energy storage (UHT-LHTES) system using Phase Change Materials (PCM) and Thermophotovoltaic (TPV) cells, creating a Solar-to-Heat-to-Power (S2H2P) storage system ten times more compact than traditional CSP storage. This innovative solution aligns with the European strategy's focus on renewable energy source (RES) flexibility and dispatchability. To optimise this complex system, COMSOL Multiphysics® 6.1 facilitates multiphysics coupling, enabling key parameter optimisation and shape improvements. The results support the selection of the best materials and design configurations. For instance, just with very simple adjustments in the angle of a wall, the system yielded an improvement of 6% by reducing the PCM melting time. This is the first time that an innovative design of this kind has been simulated with a complete CFD model for all the elements compounding the innovative S2H2P system.

Keywords: *multiphysics optimisation modelling, solar-to-heat-to-power, thermal energy storage, phase change materials, concentrated solar power, dispatchability, renewable energies, thermophotovoltaic.*

1. INTRODUCTION

As Europe carries out its ambitious Green Deal transformation towards the 2030 and 2050 energy goals, two main problems arise: dispatchability and flexibility of renewable energy sources (RES) [1]. The intermittent nature of solar and wind energy production, which comprised over a fifth of the electricity generation in 2022 [2], makes it necessary to develop long-term solutions for storing excess energy in high-production periods. Energy storage is vital for enhancing energy system flexibility, ensuring a secure supply, and promoting renewable energy integration while reducing reliance on gas power plants [3].

With solar energy production growing at increasing rates throughout Europe [4], [5], centring attention towards its intermittency problem is of utmost importance. In this regard, concentrated solar power (CSP) can provide better long-term solutions than photovoltaics thanks to thermal energy storage (TES) systems that, as M.I. Khan *et al.* (2022) [6] explain, provide precise control and stability in electrical power even during low or no sunlight, and can be more affordable than directly storing electricity with Li-ion batteries. Moreover, combining TES with energy converters such as thermophotovoltaic (TPV) cells has the potential to achieve output electric energy densities close to state-of-the-art lithium-ion batteries [7], [8], making TES and CSP key technologies in the pursuit of a more sustainable future. In this regard, the potential of integrating Power-to-Heat and TES technologies has been both analytically and experimentally explored as solutions to improve the energy transition, flexibility, sector coupling and industry electrification in Europe [9].

TES systems can be divided into three categories based on the mechanism for storing the energy: sensible heat storage, latent heat storage, and thermo-chemical storage [6], [10]. The former releases and stores energy by lowering or raising the temperature of the storage medium, while the latter can store thermal energy through endothermic fuel oxidation reactions in chemical processes [6]. Latent heat thermal energy storage

P. Droege and L. Quint (eds.), *Proceedings of the International Renewable Energy Storage and Systems Conference (IRES 2023)*, Atlantis Highlights in Engineering 32,
https://doi.org/10.2991/978-94-6463-455-6_18

(LHTES), however, takes advantage of the latent heat stored when the phase of the storage medium changes, thus achieving higher energy storage densities than the conventional sensible heat storage technologies [11]. Moreover, as phase changes occur over a small range of temperatures, LHTES can be useful for applications for which temperatures need to remain constant, while being able to store and release energy on demand [12]. However, applications for high-temperature storage are very limited due to the challenges and limitations of working at those high levels [13].

Materials used for latent heat storage are called phase change materials (PCMs). A detailed multicriteria evaluation of the PCMs thermo-physical properties and cyclability, as well as economic and sustainability aspects are crucial for a proper selection [14], [15]. There are three main types of PCMs: organic, inorganic, and eutectic mixtures [16]. Organic PCMs have major drawbacks when used in high-temperature applications, such as low latent heat values and thermal conductivity, which make the system less efficient [17]. Moreover, usually these materials also break down, are very flammable, and are more expensive than their counterparts [18]. Inorganic PCMs, such as silicon and boron, exhibit a higher melting point compared to their organic counterparts[19]. This characteristic enables the development of ultra-high temperature latent heat storage (UHT-LHTES) systems, operating over 1000ºC, that exhibit notable characteristics such as increased energy densities and improved operational efficiencies [20].

The Solar-to-Heat-to-Power (S2H2P) solution, as described by A. Datas *et al.* [7], encompasses the integration of the aforementioned concepts (CSP, TPV and UHT-LHTES with PCM). This solution also serves as the foundation for the SUNSON project [21]. The system under consideration is distinguished by its utilisation of a UHT-LHTES mechanism for CSP. This approach offers both flexibility and dispatchability, allowing for efficient energy storage with high energy densities. The conversion efficiencies are expected to increase with the high-temperature levels. Assuming a black body aperture, a solar-to-thermal conversion efficiency of over 70% can be attained at PCM temperatures of 1200ºC; and similarly, the thermal-to-electric conversion efficiency of TPV has the potential to reach efficiencies over 25% for individual cells range at 1200ºC [22]. Additionally, the system exhibits a compact and modular design, thereby facilitating the possibility of accommodating larger power capacities in the future if required.

The model proposed moves one step beyond the current state-of-the-art model simulations by formulating a numerical framework simulated with a comprehensive CFD model integrating each component of the system. Previous studies, such as the one performed by Veeraragavan *et al.* (2014) [23] or the one conducted by Zeneli *et al.* (2019) [24], have either neglected the consideration of natural convection or omitted the incorporation of radiative heat transfer mechanisms, and neither of them included a design optimisation study. The system, as outlined in [7], provides a foundational framework from which the modelling and optimisation endeavours of the UHT-LHTES developed under the SUNSON project will be undertaken. Consequently, the initial phase of this study involves the simulation of the aforementioned system utilising the computational platform COMSOL Multiphysics® 6.1 (hereinafter referred to as COMSOL). The system's performance will be enhanced and refined through an optimisation process, thereby deepening the comprehension of the underlying dynamics, and paving the way for novel avenues in system development. The overall methodology employed in this research involves the integration of simulation and optimisation techniques, which enables the enhancement of the functionality of the system and achieves greater clarity within the context of the research objectives.

2. SYSTEM DESCRIPTION

The primary configuration of the system, as depicted in **Figure 1**, comprises a cylindrical structure with multiple layers (from the outer wall: metal container, insulation, crucible, PCM, and inner cylinder hole with the movable TPV device). The solar input, which will provide the energy that will be stored in the PCM, can be found at the uppermost part of the system. The TPV cells, responsible for transforming the high-temperature thermal energy into electricity, are positioned at the inner centre of the cylinder. The cells are fixed to a motorised system that facilitates changing operational modes (by vertically moving up for charging mode and down for discharging mode), enabling the transition between charging and discharging (melting and solidifying, respectively) the PCM. Subsequently, the crucible's wall is positioned in direct proximity to the TPV cells, thereby facilitating efficient thermal transfer. The crucible serves as both the container for the PCM and the medium through which heat is transferred into and out of the PCM. Insulation serves to reduce heat dissipation to the surrounding environment, and it is contained within the outer wall of the system. The main characteristics and specifications of the S2H2P systems are listed in **Table 1**.

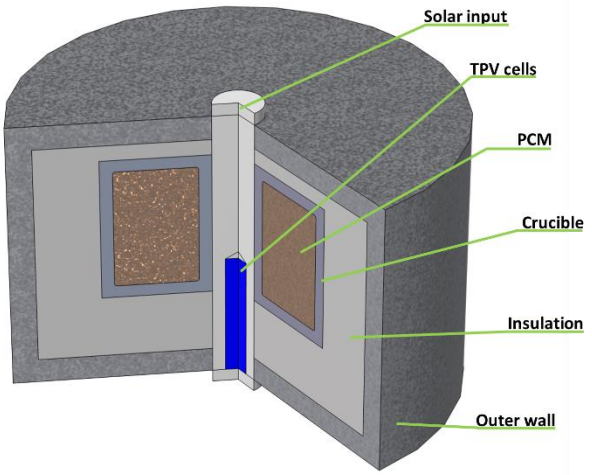

Figure 1 Conceptual image of a slice of the system.

Table 1. Main specifications and characteristics of the S2H2P system to be modelled.

Parameter	Value	Unit
P_{sol} - Solar input power	~4.4	kW
I_{sol} - Solar irradiance at the solar aperture	~350	W/cm^2
V - Volume of PCM	2.5	L
E_{th} - Stored latent heat capacity in the PCM	10350	kJ$_{th}$
k_{ins} - Insulation thermal conductivity	0.05	W/(m·K)
k_{cru} - Crucible thermal conductivity	1	W/(m·K)
$P_{d,TPV}$ - TPV cells power density generation	~1	W$_{el}$/cm^2

Pure silicon will be employed as the PCM due to its status as the Earth's second most abundant element in the crust, possession of a high melting point at elevated temperatures, and its capacity for storing substantial amounts of energy. The properties utilised are listed in **Table 2**.

Table 2 Used properties for solid and liquid silicon.

Property	Solid silicon	Liquid silicon	Reference
ρ - Density (kg/m^3)	2300		[7]
k - Thermal conductivity (W/(m·K))	25	50	[7]
C_p - Heat capacity (J/(kg·K))	1040		[7]
μ - Dynamic viscosity (Pa·s)	-	$0.9 \cdot 10^{-3}$	[25]
L_f - Latent heat of fusion (J/kg)	$1.8 \cdot 10^6$		[7]
T_m - Melting point (K)	1680		[7]

The PCM, as the core storage material, is kept in a crucible and has a volume of approximately 2.5 litres, which for silicon would hold about 10350 kJ of latent heat energy (Equation (1)).

$$E_{th} = L_f \rho V \tag{1}$$

Where L_f is the latent heat of fusion, ρ is the density of silicon, which is assumed constant for the solid and liquid phases, and V is the volume of PCM.

The total area of the TPV cells is approximately 63 cm^2. To replicate the system, a simplified approach will be adopted as outlined in [26]. This approach involves considering the heat absorbed by the TPV cells as represented by Equations (2) and (3).

$$q = -G\eta_{pv} \tag{2}$$

$$\eta_{pv} = \begin{cases} 0.2\left[1 - \left(\frac{T}{800} - 1\right)^2\right] & T \leq 1600K \\ 0 & T > 1600K \end{cases} \tag{3}$$

Where q is the heat flux, G is irradiation, and η_{pv} is the efficiency of the TPV cells as a function of temperature.

As demonstrated by **Figure 2**, the TPV has a maximum efficiency of 20% that is achieved at 800K.

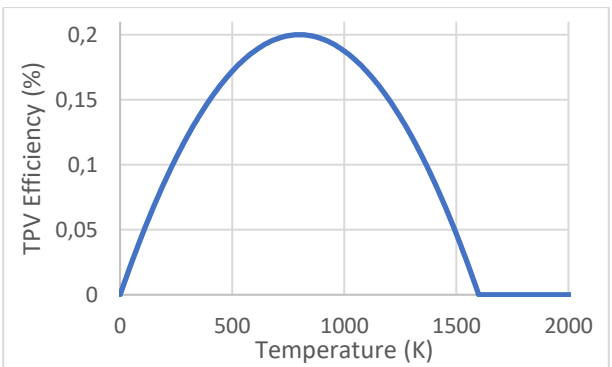

Figure 2 TPV efficiency as a function of temperature. Figure based on literature reported in [26].

3. COMSOL SIMULATION SETUP

In the realm of computational fluid dynamics (CFD) and multiphysics simulations, the utilisation of specialised software packages has become imperative for the accurate modelling and analysis of complex physical phenomena. Among the notable platforms in this domain, COMSOL stands as a versatile and robust tool capable of

addressing a wide spectrum of coupled physics problems. In this section, the essential components of a COMSOL setup are elucidated, tailored to simulate a 2D axisymmetric configuration featuring natural convection, encompassing non-isothermal flow, laminar flow, heat transfer in solids and fluids, as well as surface-to-surface radiation.

3.1 Geometry

As the system has a circular configuration, a simplification using a 2D axisymmetric simulation will be performed, meaning that only the modelling of a 2D slice of the whole system (see **Figure 3**) using a polar coordinate system (r, z) is needed. Additionally, COMSOL provides the capability to parameterise the geometry, facilitating the efficient modification of any dimension within the system to evaluate its impact on the results. This feature also allows for conducting optimisation studies, which will be further elaborated upon in subsequent sections.

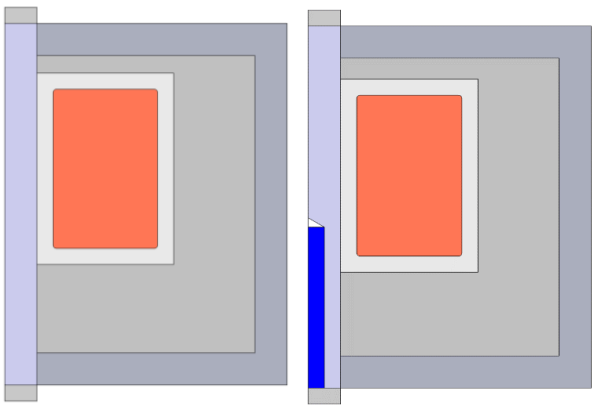

Figure 3 2D charging (top) and discharging (bottom) configurations of the system in COMSOL.

3.2 Physics Interfaces

The fidelity of the simulation hinges on selecting the appropriate physics interfaces that encapsulate the governing physical phenomena. In the context of the aforementioned 2D axisymmetric natural convection problem, several physics interfaces must be configured.

3.2.1 Laminar Flow

The Navier-Stokes equations for incompressible, laminar flow must be chosen to describe fluid motion [27]:

$$\rho\frac{\partial \boldsymbol{u}}{\partial t}+\rho(\boldsymbol{u}\cdot\nabla)\boldsymbol{u}=\nabla\cdot[-p\boldsymbol{I}+\boldsymbol{K}]+\boldsymbol{F}+\left(\rho-\rho_{ref}\right)\boldsymbol{g} \quad (4)$$

$$\rho\nabla\cdot\boldsymbol{u}=0 \quad (5)$$

$$\boldsymbol{K}=\mu(\nabla\boldsymbol{u}+(\nabla\boldsymbol{u})^{T}) \quad (6)$$

Where ρ is the density of the fluid, **u** is the velocity vector, p is pressure, **F** is an applied volume force, ρ_{ref} is the reference density, **g** is the gravity vector, pointing towards the negative z-axis, and μ is the dynamic viscosity. All are in SI units.

To perform the simulation, it is required to assign the laminar flow domain to the PCM. However, at the beginning of the simulation, the domain is solid, meaning the velocity should be 0, which is not accounted for by default. Moreover, the change from solid to liquid is not instantly defined, meaning there is a "mushy zone" where the material is partially solidified and liquefied, resembling a porous material [28]. This mushy zone exists in the PCM in a range (transition interval) of 4 K centred around the melting point of silicon, which has been defined as small enough to capture the proper phase change but not too small for numerical reasons, as the smaller the transition interval, the more difficult it is for the simulation to converge.

To account for the mushy zone, it is necessary to assign a volume force **F** to the PCM domain to dampen the velocity at the phase-change interface, which will be defined as seen in Equation (7) [29].

$$\boldsymbol{F}=-\frac{(1-\alpha)^2}{\alpha^3+\delta}A_{mush}\boldsymbol{u} \quad (7)$$

Where α is the volume fraction of the liquid phase, δ is a small constant used to avoid division by zero, and A_{mush} is the mushy zone parameter, which depends on the morphology of the melting front. This constant is usually large, around 10^4-10^7 [30]. In the present study, values of $A_{mush}=6\cdot10^4\ \frac{kg}{m^3\cdot s}$ and $\delta=0.001$ will be used, as utilised in [31].

3.2.2 Heat Transfer in Fluids and Solids and Non-isothermal Flow

To simulate the natural convection of the liquid PCM, the thermal transfer equations need to be solved (Equations (8-10)) [32].

$$\rho C_p\frac{\partial T}{\partial t}+\rho C_p\boldsymbol{u}\cdot\nabla\mathrm{T}+\nabla\cdot\boldsymbol{q}=Q+Q_{vd} \quad (8)$$

$$\boldsymbol{q}=-k\nabla\mathrm{T} \quad (9)$$

$$Q_{vd}=\boldsymbol{\tau}:\nabla\boldsymbol{u} \quad (10)$$

Where C_p is the heat capacity at constant pressure, Q are heat sources other than viscous dissipation in the fluid (Q_{vd}), and $\boldsymbol{\tau}$ is the viscous stress tensor.

To solve for the thermal transfer of solids, Equations (8) and (9) will be used while ignoring the viscous dissipation term.

The Boussinesq approximation, which is frequently employed for the purpose of simulating flows driven by buoyancy [27], will be employed to address the natural convection of an incompressible fluid. It assumes that buoyancy effects are solely attributed to density variations, and Equation (11) delineates the gravitational force attributed to the approximation.

$$\boldsymbol{F_g}=\rho_{ref}\left(1-\alpha_{p,0,ref}\right)\left(T-T_{ref}\right)\boldsymbol{g} \quad (11)$$

3.2.3 Surface-to-Surface Radiation

Surface-to-surface radiation plays a crucial role in systems involving high temperatures or radiating surfaces. By enabling the radiation module, one can accurately account for radiative heat transfer between different surfaces within the domain. The following equations will be solved, which have been extracted from the Heat Transfer Module's user guide [32]:

$$J = \varepsilon e_b(T) + \rho_d G \quad (12)$$

$$\varepsilon + \rho_d = 1 \quad (13)$$

$$G = G_m \quad (14)$$

$$e_b(T) = n^2 \sigma T^4 \quad (15)$$

$$q_{r,net} = \varepsilon\big(G - e_b(T)\big) \quad (16)$$

Where J is radiosity, ε is emissivity, ρ_d is diffuse reflectivity, $e_b(T)$ is the power radiated across all wavelengths, G_m is mutual irradiation, n is the refractive index, and σ is the Stefan-Boltzmann constant ($5.67 \cdot 10^{-8}$ J/(s·m^2·K^4)).

3.2.4 Mesh Independence Study and Time Step

In the realm of the Finite Element Method, employed by COMSOL for geometry discretisation and equation resolution within individual mesh elements, an important aspect arises—namely, the solution's sensitivity to the mesh employed.

In order to guarantee precision in the solution, a thorough exploration of mesh independence is undertaken in this study. This involves solving the identical model across progressively refined meshes to determine an optimal size for subsequent analyses. Striking a balance between solution accuracy and computational efficiency becomes imperative in this process.

In the default case (with a 90º crucible wall), four different mesh sizes were tested. The focus was on the PCM domain, as the CFD simulation is particularly sensitive to the mesh, especially during the melting process. The three default sizes in COMSOL used are normal, finer, and extremely fine, while the finest size is a custom mesh with a maximum PCM domain element size of 0.78 mm.

As demonstrated in **Figure 4**, there is no perceptible difference in the melting time or the melting curve characteristics between the extremely fine and the finest mesh sizes. Thus, a mesh size of the default setting "extremely fine" will be used for the following simulations.

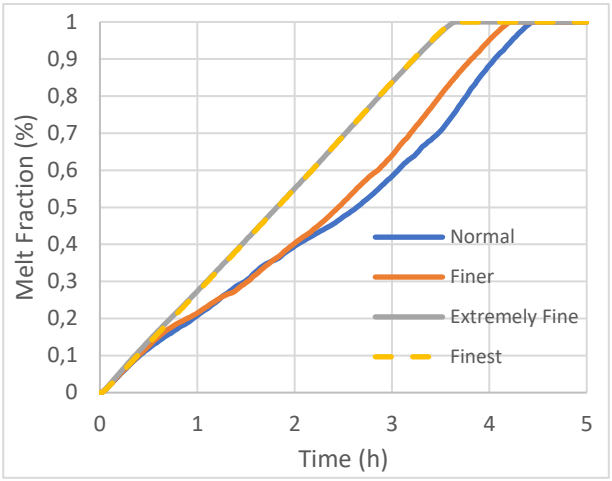

Figure 4 Melt fraction for each mesh size.

Figure 5 shows the resulting meshes, which are formed by both triangles and quadrilaterals (quads), the latter utilised for the inner walls of the crucible to aid in the CFD simulations.

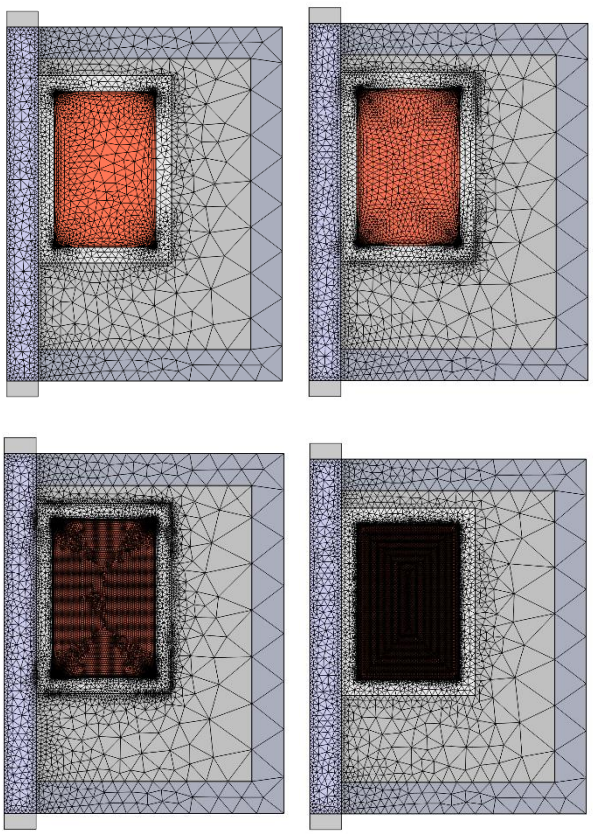

Figure 5 Mesh visualisation for sizes normal (top-left), finer (top-right), extremely fine (bottom-left), and finest (bottom-right).

The main properties of each mesh are displayed in **Table 3**.

Table 3 Main properties of the studied meshes.

Mesh size	Number of triangles	Number of quads	Maximum triangle size inside PCM domain [mm]
Normal	5158	312	7.88
Finer	7370	412	4.9
Extremely Fine	21608	732	1.17
Finest	31140	832	0.78

Not only does COMSOL discretise space with a mesh to solve the equations, but it also discretises time. However, it has been found that the automatic time-stepping method included in the software gives accurate results, so that method will be used for the simulations. This can be seen in **Figure 6**, where the same simulation of the base geometry has been performed with different maximum time steps.

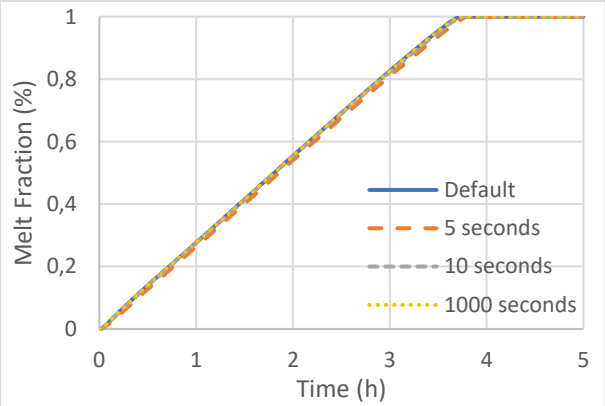

Figure 6 Melt fraction comparison for simulations with different maximum time steps.

3.2.4 Boundary conditions

The boundary and initial conditions used to solve the simulations are presented in **Table 4** and in **Figure 7**.

Table 4 Boundary conditions.

Boundary	CFD condition	Heat transfer condition
Crucible wall	No slip	-
Air, crucible and PCM	-	Initial temperature 1400ºC
Insulation	-	Initial temperature 1000ºC
Outer wall	-	Initial temperature 460ºC
Outer lateral and upper walls	-	Convective heat flux with heat transfer coefficient 10 W/(m^2·K) and external temperature 20ºC
		Surface-to-Ambient radiation with ambient temperature 20ºC
Walls highlighted in Figure 7	-	Diffusive surfaces

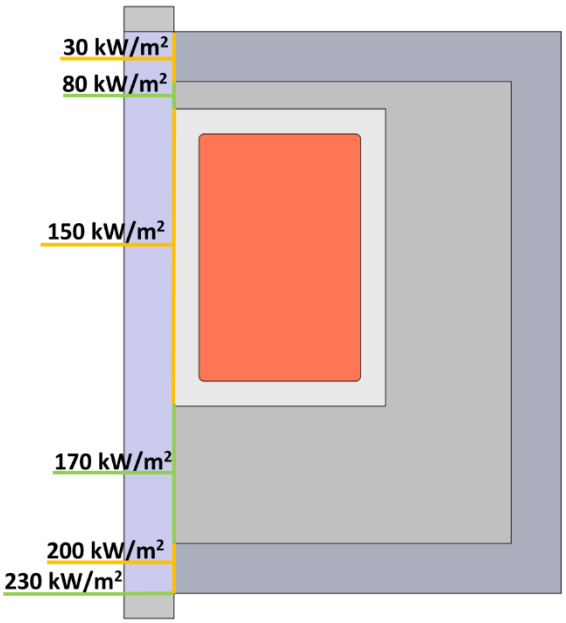

Figure 7 Boundary heat sources simulating the concentrated solar power.

3.2.5 Optimisation in COMSOL

In order to adjust the design parameters—geometric, material, or operational—within the specific S2H2P system model, the present study will employ the parameter optimisation tool, which allows the systematic variation of model parameters while targeting specific performance objectives. In this sense, COMSOL presents useful optimisation capabilities for novel designs, such as parametric analysis, shape, and topology optimisation [33]. By defining design parameters and objective functions, COMSOL facilitates the exploration of parameter spaces, enabling the identification of optimal configurations based on predefined criteria.

Specifically in the present work, parameter optimisation will be used to adjust the crucible's shape and geometry: the slope of the wall closest to the TPV cells will be modified while ensuring that the volume of the PCM remains unchanged. The purpose of implementing this optimisation is to maintain an easily manufacturable crucible design while improving the most essential attributes of the system. The focus of this article is to improve the charging time of the system, specifically the melting process of the PCM, to enhance flexibility in rapidly changing conditions. In the discharging phase, the objective is to maximise the efficiency of the TPV cell to increase electricity production. The existing geometric configuration permits a wall inclination ranging from 85° to 95° relative to the horizontal, as depicted in **Figure 8**, so that range will mark the bounds of the optimisation procedure.

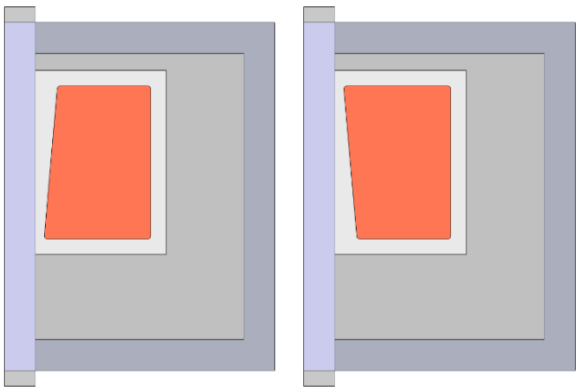

Figure 8 System with the left wall of the crucible forming with the horizontal 85° (left) and 95° (right).

3.2.6 Validation

In the context of the current research, a validation exercise has been carried out to evaluate the accuracy of the COMSOL setup proposed by contrasting its outcomes with those reported in a previously published work (hereafter referred to as the reference study) [34]. This validation procedure is essential for proving the validity and applicability of the simulation framework and, consequently, for boosting trust in the subsequent analyses and conclusions.

3.2.6.1 Reference Study and Benchmark Data

The reference study encompasses several experimental configurations involving a cuboid made of a PCM, which is subjected to heating through a sequence of electrical resistances. A metal plate with an angled fin, which is in contact with the material, is provided as an attachment. In each experimental trial, the angle of the fin is varied. The authors additionally conduct a numerical simulation of the system using COMSOL. Upon conducting both investigations, the researchers proceeded to compare the results and ultimately deduced that the numerical simulation closely approximates the findings of the experimental study.

To determine the fidelity of the approach employed in the current study in accurately replicating the phenomena under investigation, an identical geometry as the reference study will be utilised, albeit with the configuration specific to the present UHT-LHTES CSP system. **Figure 9** shows the geometry of the reference study implemented in COMSOL.

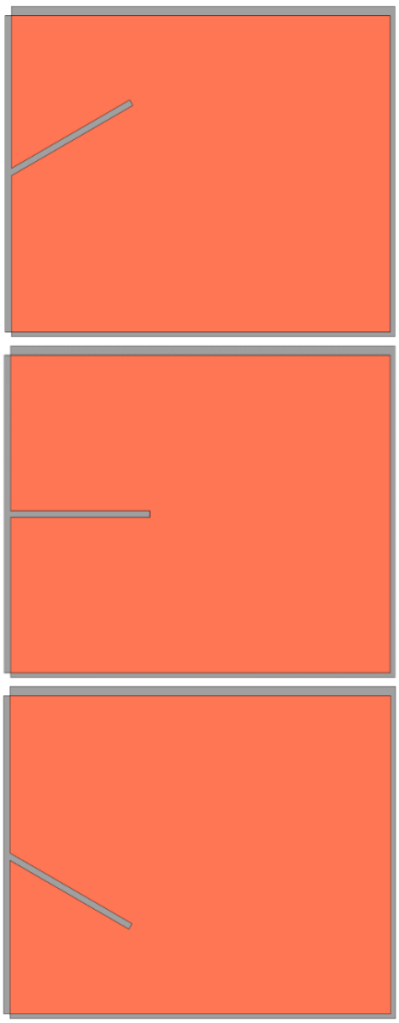

Figure 9 Setup of the validation simulation with: -30° fin (top), horizontal fin (middle), and -30° fin (bottom).

The average melt fraction with respect to time will be used as a benchmark, as it is the most important characteristic of a PCM system related to the charging and discharging timing.

3.2.6.2 Comparison of Results

The conformity between the COMSOL configuration of the present study for the natural convection and melting of the PCM, as depicted in **Figure 10**, is evident in its alignment with both the numerical simulation and experimental investigation conducted in the reference study. To further assess the results, the root-mean-square

deviation (RMSD) has been calculated for all measures of the differences between the developed model and the experimental and numerical predicted values of the reference investigation. In general, a lower RMSD is better than a higher one, and a close value to zero would indicate a perfect fit to the data.

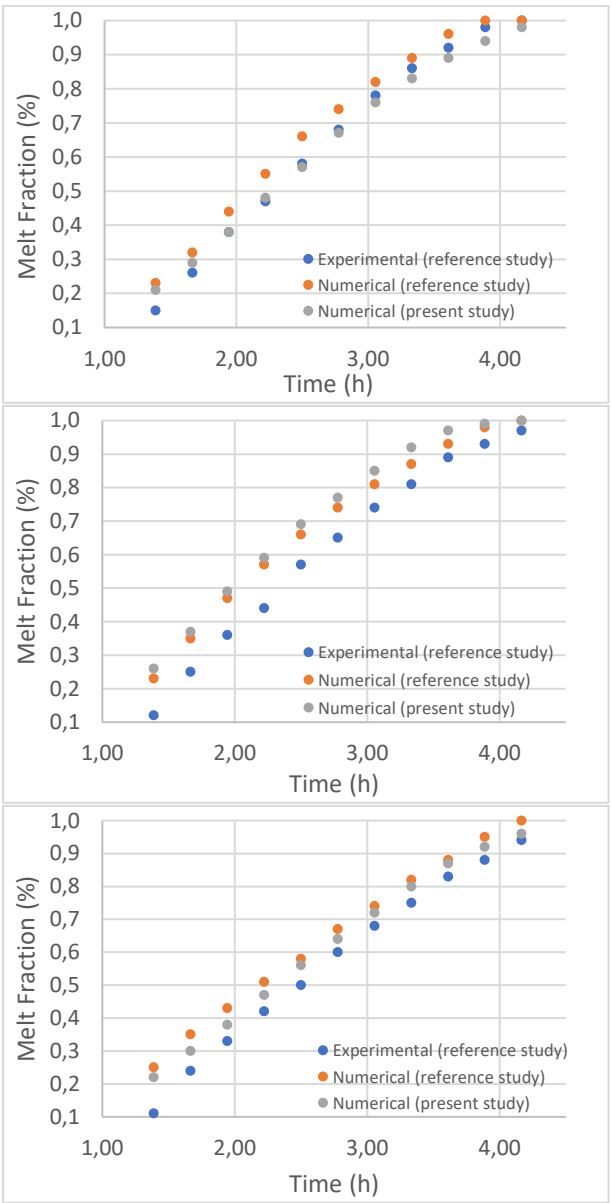

Figure 10 Melt fraction comparison of system with: 30° fin (top), horizontal fin (middle), -30° fin (bottom) against the results adapted from the reference study [34].

The RMSD values of both numerical models vary in the range from 0.03 and 0.06 for the three study cases (-30º, 0º, +30º angle fins). Regarding the comparison with the experimental results, the error of our model slightly increased for the 0º angle fin, up to 0.11. Conversely, the developed model provided more accurate results for the other two cases (-30º and +30º angles), relevantly decreasing the RMSD 50% and 33%, respectively. Overall, based on the findings of the validation comparative analysis, the methodology described is assumed to be adequate to be employed for conducting the COMSOL simulation of the system under investigation in the present study.

4. DISCUSSION AND ANALYSIS OF RESULTS

The system configuration outlined in Section 3 is implemented to conduct the optimisation process and validate the outcomes using the nearest integer angle. In order to assess the outcomes, a comparative analysis will be conducted on the optimal (86º), suboptimal (91º), and baseline (90º) scenarios.

Upon the results for the charging process, it is evident from the comparative analysis depicted in **Figure 11** that the optimised geometry featuring an 86° wall exhibits a 6% enhancement in charging times in comparison to the baseline scenario with a 90° wall, and a 9% improvement over the worst case scenario of a 91° wall.

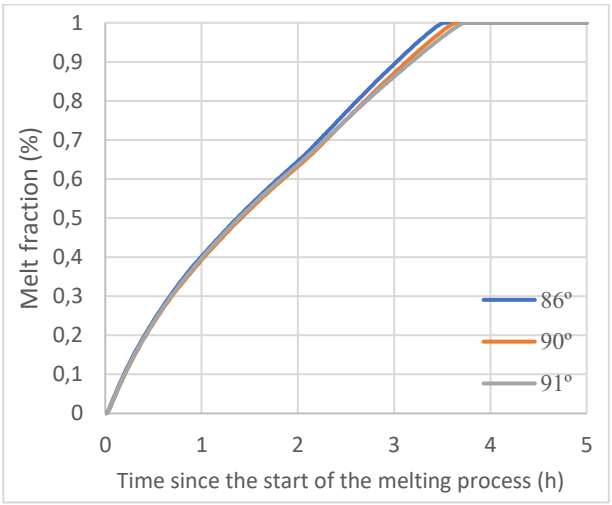

Figure 11 Comparison of melt fraction results of the charging simulation.

Figure 12 visually represents the melting fronts and velocity field at the 1-hour mark, allowing for a comparative analysis. The melting front starts as a vertical wall that moves outwards, but eventually, the formation of a whirl at the top of the container can be observed. It can be attributed to the buoyancy effects, a phenomenon that occurs due to the higher temperature of the molten PCM in proximity to the left wall, causing it to ascend towards the top.

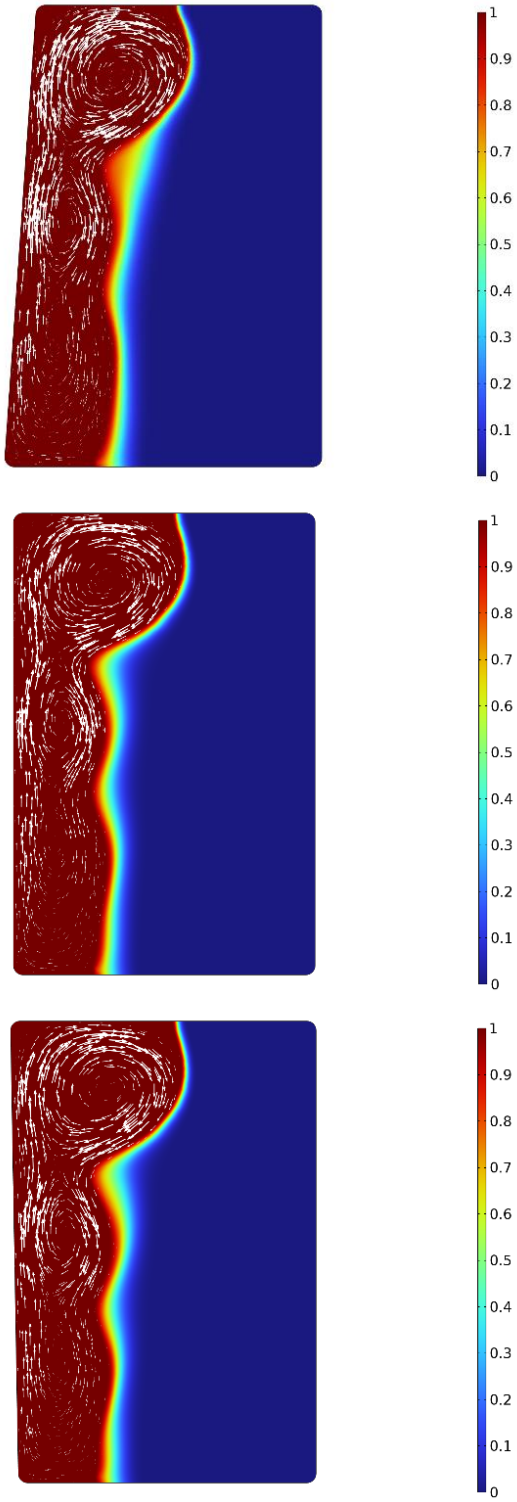

Figure 12 Melt fraction at 1 hour and velocity field (arrows) with left wall at 86º (top), 90º (middle) and 91º (bottom).

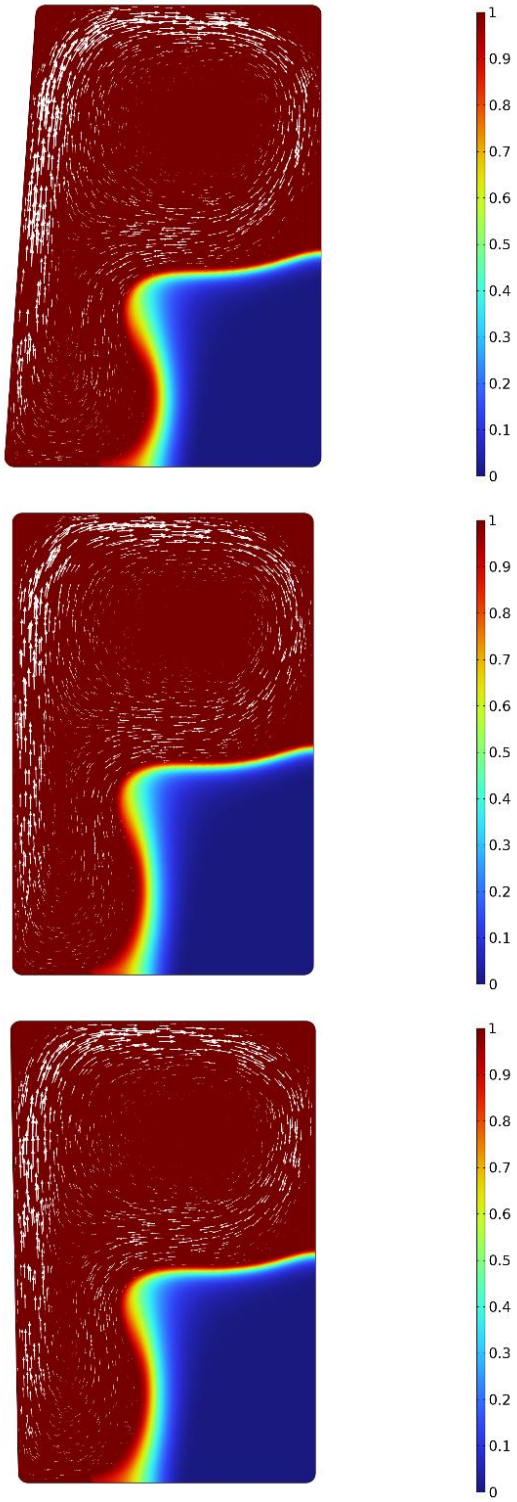

Figure 13 Melt fraction at 2.5 hours and velocity field (arrows) with left wall at 86º (top), 90º (middle) and 91º (bottom).

Similarly, **Figure 13** illustrates the melting front and velocity fields of the various configurations after a duration of 2.5 hours. The aforementioned whirl is observable at the upper region, albeit on a larger scale, accompanied by an increase in the velocity field for the case at 86º.

Finally, **Figure 14** illustrates the melting front and velocity field of the various designs after 4 hours. It is evident that the 86º case has almost completely melted, whilst the remaining cases have not undergone the same degree of melting.

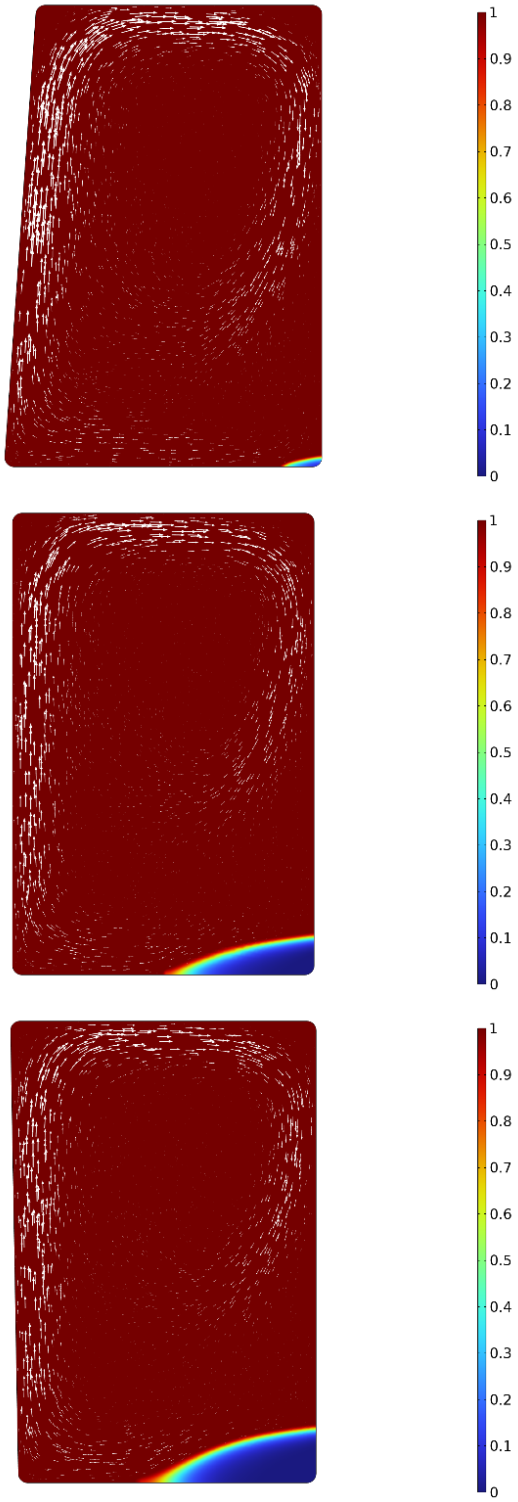

Figure 14 Melt fraction at 3.5 hours and velocity field (arrows) with left wall at 86º (top), 90º (middle) and 91º (bottom).

This characteristic melting front, with the appearance of whirls, is achieved by the inclusion of buoyancy effects, without which the melting front would have a more linear behaviour.

The analysis of the discharging process does not exhibit any substantial differences across the various geometries, as illustrated in **Figure 15**. This may be due to the fact that solidification is a conduction-dominated process [35]. The result suggests that the usage of the 86° wall would benefit the charging process and lead to an increase in the electrical output power of around 5%, being approximately 0.9 kWh for every discharging cycle performed. The estimated annual electricity generation, taking into account both charging and discharging cycles, is projected to vary between 400 and 500 kWh, considering the power and dimensions of the simulated prototype.

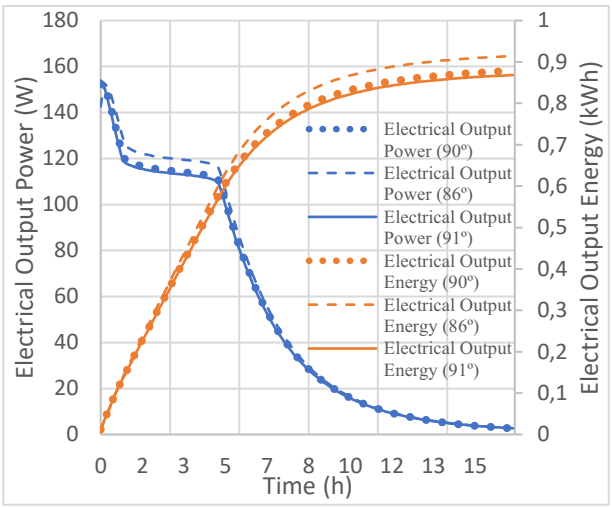

Figure 15 Comparison of electrical output power of the discharging simulation.

5. CONCLUSION

The present study specifies a conceptual framework for a UHT-LHTES system, which utilises CSP technology to induce the phase transition of an inorganic PCM, specifically silicon. Subsequently, TPV cells effectively convert the stored thermal energy into electrical energy, exhibiting notable attributes such as high energy densities, compactness, scalability, dispatchability, and flexibility. These characteristics make the presented system a valuable contributor to the European Union's renewable energy climate objectives for the years 2030 and 2050.

The COMSOL model developed enables simulations with methods, applications, and equations pertinent to the UHT-S2H2P system's specific application. This represents the very first simulation of an innovative design utilising a comprehensive CFD model to represent all the S2H2P system's components by integrating a numerical framework that simulates a complete CFD model to facilitate the modelling and optimisation.

In the early design stages, the model's capacity to accurately replicate and reproduce these specific variables makes it a valuable tool. This assertion holds

particular validity in the context of innovative systems, wherein the level of uncertainty and risk tends to be elevated owing to the absence of prior data or experience with these novel designs. Therefore, this circumstance contributes to the enhancement of the overall effectiveness and cost-effectiveness by supporting the design process (adaption configuration parameters and constructive elements for heat transference enhancement as the fins) and system operation (electricity generation and cycles adaptation).

The charging and discharging processes are simulated by utilising the COMSOL software. This has allowed the inclusion of the representation of the melt fraction of the PCM, as well as the examination of its performance throughout the processes of charging and discharging. Based on this information, it is feasible to identify crucial areas that need to be considered during the design phase. These areas may include regions that are more challenging to melt, necessitating adjustments in the geometry and shape of the system or the addition of fins to enhance heat transfer. Overall, the design is optimised to enhance the charging times by reducing the period to melt the PCM of the storage unit, to increase its flexibility and adaptability, resulting in a 6% improvement. Moreover, regarding the discharging process, an increase of around 5% has been found for the best case. It is important to highlight that these enhancements have been accomplished by adjusting a minor parameter that falls within engineering and manufacturing feasibility. Specifically, the wall angle, which can be easily modified without significant economic consequences, has been adapted to yield advantageous design outcomes.

In this sense, the design that has been presented in this article will serve as an initial iteration for the S2H2P system in the SUNSON project. From that point, it will undergo further optimisation to attain the project objectives. To simulate and optimise their design in a virtual environment prior to physical manufacturing, these simulations may incorporate varying real-world conditions and boundary conditions to ease the upscaling process. For instance, further additional efforts encompass the optimisation of the crucible's shape, the charging/discharging strategy, as well as the selection of materials and the arrangement of key system components (i.e., TPV converter, solar aperture control).

AUTHORS' CONTRIBUTIONS

Alfonso Hernández: investigation, formal analysis, data curation, visualisation, writing – original draft. Luis E. Acevedo: conceptualisation, investigation, review and resources. Ignacio Fernández-Pacheco: visualisation, review and editing. Patricia Royo: conceptualisation, methodology, formal analysis, review, editing, supervision, project administration and funding acquisition.

ACKNOWLEDGMENTS

The authors extend their thanks to the funding received from the SUNSON project funded by the European Commission, Horizon Europe Programme under Grant Agreement nº101083827.

DISCLAIMER

LIST OF SYMBOLS

A_{mush}	Mushy zone parameter [kg/(m^3·s)]
C_p	Heat capacity [J/(kg·K)]
$e_b(T)$	Power radiated across all wavelengths [W/m^2]
E_{th}	Stored latent heat capacity in the PCM [J_{th}]
F	Applied volume force [kg·m/s^2]
G	Irradiation [W/m^2]
G_m	Mutual irradiation [W/m^2]
g	Gravity vector [m/s^2]
I	Identity tensor [-]
I_{sol}	Solar irradiance at the solar aperture [W/m^2]
J	Radiosity [W/m^2]
K	Viscous stress tensor [kg/(m·s^2)]
k	Thermal conductivity [W/(m·K)]
k_{cru}	Crucible thermal conductivity [W/(m·K)]
k_{ins}	Insulation thermal conductivity [W/(m·K)]
L_f	Latent heat of fusion [J/kg]
n	Refractive index [-]
p	Pressure [kg/(m·s^2)]
$P_{d,TPV}$	TPV cells' power density generation []
P_{sol}	Solar input power [W]
q	Heat flux [W/m^2]
$q_{r,net}$	Net radiative heat flux [W/m^2]
Q	Heat source [W/m^3]
Q_{vd}	Viscous dissipation [W/m^3]
T	Temperature [K]
T_{ref}	Reference Temperature [K]
T_m	Melting point [K]
t	Time [s]

u	Velocity vector [m/s]
V	Volume of the PCM [m^3]

GREEK SYMBOLS

α	Volume fraction of the liquid phase [-]
$\alpha_{p,0,ref}$	Reference coefficient of thermal expansion [1/K]
δ	Large arbitrary constant linked to the volume force definition [-]
ε	Emissivity [-]
η_{pv}	Efficiency of TPV cells [-]
μ	Dynamic viscosity [kg/(m·s)]
ρ	Density of PCM [kg/m^3]
ρ_d	Diffuse reflectivity [-]
ρ_{ref}	Reference density [kg/m^3]
σ	Stefan-Boltzmann constant [$J/(s \cdot m^2 \cdot K^4)$]
τ	Viscous stress tensor

ABBREVIATIONS

CFD	Computational Fluid Dynamics
CSP	Concentrated Solar Power
LHTES	Latent Heat Thermal Energy Storage
PCM	Phase Change Material
RES	Renewable Energy Source
RMSD	Root-Mean-Square Deviation
S2H2P	Solar-to-Heat-to-Power
TES	Thermal Energy Storage
TPV	Thermophotovoltaic
UHT	Ultra-High Temperature

REFERENCES

[1] "Future EU power systems: renewables' integration to require up to 7 times larger flexibility." Accessed: Sep. 21, 2023. [Online]. Available: https://joint-research-centre.ec.europa.eu/jrc-news-and-updates/future-eu-power-systems-renewables-integration-require-7-times-larger-flexibility-2023-06-26_en

[2] "Wind and solar overtake fossil gas to produce record fifth of EU electricity | Ember." Accessed: Sep. 21, 2023. [Online]. Available: https://ember-climate.org/press-releases/wind-and-solar-overtake-fossil-gas-to-produce-record-fifth-of-eu-electricity/

[3] "EUR-Lex - 52022DC0230 - EN - EUR-Lex." Accessed: Sep. 29, 2023. [Online]. Available: https://eur-lex.europa.eu/legal-content/EN/TXT/?uri=COM%3A2022%3A230%3AFIN

[4] "EU Market Outlook For Solar Power."

[5] A. CHATZIPANAGI *et al.*, "Clean Energy Technology Observatory: Photovoltaics in the European Union – 2022 Status Report on Technology Development, Trends, Value Chains and Markets," *Publications Office of the European Union*, 2022, doi: 10.2760/812610.

[6] M. I. Khan, F. Asfand, and S. G. Al-Ghamdi, "Progress in research and technological advancements of thermal energy storage systems for concentrated solar power," *J Energy Storage*, vol. 55, p. 105860, Nov. 2022, doi: 10.1016/J.EST.2022.105860.

[7] A. Datas, A. Ramos, A. Martí, C. del Cañizo, and A. Luque, "Ultra high temperature latent heat energy storage and thermophotovoltaic energy conversion," *Energy*, vol. 107, pp. 542–549, Jul. 2016, doi: 10.1016/J.ENERGY.2016.04.048.

[8] T. Burger, C. Sempere, B. Roy-Layinde, and A. Lenert, "Present Efficiencies and Future Opportunities in Thermophotovoltaics," *Joule*, vol. 4, no. 8, pp. 1660–1680, Aug. 2020, doi: 10.1016/J.JOULE.2020.06.021.

[9] P. Royo *et al.*, "Experimental analysis of a power-to-heat storage with high-temperature phase change materials to increase flexibility and sector coupling," *Appl Therm Eng*, vol. 236, p. 121889, Jan. 2024, doi: 10.1016/J.APPLTHERMALENG.2023.121889.

[10] A. Palacios, M. E. Navarro-Rivero, B. Zou, Z. Jiang, M. T. Harrison, and Y. Ding, "A perspective on Phase Change Material encapsulation: Guidance for encapsulation design methodology from low to high-temperature thermal energy storage applications," *J Energy Storage*, vol. 72, p. 108597, Nov. 2023, doi: 10.1016/J.EST.2023.108597.

[11] M. Opolot, C. Zhao, M. Liu, S. Mancin, F. Bruno, and K. Hooman, "A review of high temperature (≥ 500 °C) latent heat thermal energy storage," *Renewable and Sustainable Energy Reviews*, vol. 160, p. 112293, May 2022, doi: 10.1016/J.RSER.2022.112293.

[12] E. N. Kumi, "Energy storage technologies," *Pumped Hydro Energy Storage for Hybrid Systems*, pp. 1–21, Jan. 2023, doi: 10.1016/B978-0-12-818853-8.00002-9.

[13] P. Royo, L. Acevedo, V. J. Ferreira, T. García-Armingol, A. M. López-Sabirón, and G. Ferreira, "High-temperature PCM-based thermal energy

storage for industrial furnaces installed in energy-intensive industries," *Energy*, vol. 173, pp. 1030–1040, Apr. 2019, doi: 10.1016/J.ENERGY.2019.02.118.

[14] P. Royo, V. J. Ferreira, Z. Ure, S. Gledhill, A. M. López-Sabirón, and G. Ferreira, "Multiple-Criteria Decision Analysis and characterisation of phase change materials for waste heat recovery at high temperature for sustainable energy-intensive industry," *Mater Des*, vol. 186, p. 108215, Jan. 2020, doi: 10.1016/J.MATDES.2019.108215.

[15] P. Royo *et al.*, "Decision Support System of Innovative High-Temperature Latent Heat Storage for Waste Heat Recovery in the Energy-Intensive Industry," *Energies 2021, Vol. 14, Page 365*, vol. 14, no. 2, p. 365, Jan. 2021, doi: 10.3390/EN14020365.

[16] M. Mhadhbi and M. Mhadhbi, "Introductory Chapter: Phase Change Material," *Phase Change Materials and Their Applications*, Aug. 2018, doi: 10.5772/INTECHOPEN.79432.

[17] M. Casini, "Phase-change materials," *Smart Buildings*, pp. 179–218, Jan. 2016, doi: 10.1016/B978-0-08-100635-1.00005-8.

[18] F. Bruno, M. Belusko, M. Liu, and N. H. S. Tay, "Solid-liquid phase change materials for thermal energy storage," *Advances in Thermal Energy Storage Systems: Methods and Applications*, pp. 221–268, Jan. 2021, doi: 10.1016/B978-0-12-819885-8.00009-7.

[19] J. Safarian and M. Tangstad, "Phase change materials for high-temperature operation," *Ultra-High Temperature Thermal Energy Storage, Transfer and Conversion*, pp. 85–111, Jan. 2021, doi: 10.1016/B978-0-12-819955-8.00004-1.

[20] A. Ramos, E. López, C. del Cañizo, and A. Datas, "Cost-effective ultra-high temperature latent heat thermal energy storage systems," *J Energy Storage*, vol. 49, p. 104131, May 2022, doi: 10.1016/J.EST.2022.104131.

[21] "Concentrated Solar energy storage at Ultra-high temperatures aNd Solid-state cONversion | SUNSON | Project | Fact sheet | HORIZON | CORDIS | European Commission." Accessed: Sep. 25, 2023. [Online]. Available: https://cordis.europa.eu/project/id/101083827

[22] E. J. Tervo *et al.*, "Efficient and scalable GaInAs thermophotovoltaic devices," *Joule*, vol. 6, no. 11, pp. 2566–2584, Nov. 2022, doi: 10.1016/j.joule.2022.10.002.

[23] A. Veeraragavan, L. Montgomery, and A. Datas, "Night time performance of a storage integrated solar thermophotovoltaic (SISTPV) system," *Solar Energy*, vol. 108, pp. 377–389, Oct. 2014, doi: 10.1016/J.SOLENER.2014.07.005.

[24] M. Zeneli *et al.*, "Numerical simulation of a silicon-based latent heat thermal energy storage system operating at ultra-high temperatures," *Appl Energy*, vol. 242, pp. 837–853, May 2019, doi: 10.1016/J.APENERGY.2019.03.147.

[25] H. Sasaki, E. Tokizaki, X. M. Huang, K. Terashima, and S. Kimura, "Temperature dependence of the viscosity of molten silicon measured by the oscillating cup method," *Jpn J Appl Phys*, vol. 34, no. 7R, pp. 3432–3436, Jul. 1995, doi: 10.1143/JJAP.34.3432/XML.

[26] Comsol, "Heat Transfer Module Application Library," 2021, Accessed: Sep. 26, 2023. [Online]. Available: www.comsol.com/trademarks.

[27] Comsol, "The CFD Module User's Guide," 2022, Accessed: Sep. 27, 2023. [Online]. Available: www.comsol.com/blogs

[28] V. R. Voller and C. Prakash, "A fixed grid numerical modelling methodology for convection-diffusion mushy region phase-change problems," *Int J Heat Mass Transf*, vol. 30, no. 8, pp. 1709–1719, Aug. 1987, doi: 10.1016/0017-9310(87)90317-6.

[29] V. R. Voller and C. Prakash, "A fixed grid numerical modelling methodology for convection-diffusion mushy region phase-change problems," *Int J Heat Mass Transf*, vol. 30, no. 8, pp. 1709–1719, Aug. 1987, doi: 10.1016/0017-9310(87)90317-6.

[30] V. Shatikian, G. Ziskind, and R. Letan, "Numerical investigation of a PCM-based heat sink with internal fins," *Int J Heat Mass Transf*, vol. 48, no. 17, pp. 3689–3706, Aug. 2005, doi: 10.1016/J.IJHEATMASSTRANSFER.2004.10.042.

[31] Comsol, "Continuous Casting-Apparent Heat Capacity Method," 2021, Accessed: Oct. 09, 2023. [Online]. Available: www.comsol.com/trademarks.

[32] Comsol, "The Heat Transfer Module User's Guide," 2022, Accessed: Sep. 27, 2023. [Online]. Available: www.comsol.com/blogs

[33] Comsol, "The Optimization Module User's Guide," 2022, Accessed: Sep. 27, 2023. [Online]. Available: www.comsol.com/blogs

[34] Z. Qin, Z. H. Low, C. Ji, and F. Duan, “Efficacy of angled metallic fins for enhancing phase change material melting,” *International Communications in Heat and Mass Transfer*, vol. 132, p. 105921, Mar. 2022, doi: 10.1016/J.ICHEATMASSTRANSFER.2022.105921.

[35] X. Gao, W. Zhang, Z. Fang, X. Hou, and X. Zhang, “Analysis of melting and solidification processes in the phase-change device of an energy storage interconnected heat pump system,” *AIP Adv*, vol. 10, no. 5, p. 55021, May 2020, doi: 10.1063/5.0006280/21364.